https://doi.org/10.5194/egusphere-2026-2264
Preprint. Discussion started: 8 July 2026

Improving representativeness of microwave radiometer brightness temperatures for data assimilation by complementing cloud detection with cloud clearing

Moritz Löffler[1,3] , Christine Knist[2,] , Bernhard Pospichal[3,] , and Ulrich Löhnert[3,]

[1]German Weather Service (DWD), Technical Infrastructure and Operations, 14473 Potsdam, Germany
[2]German Weather Service (DWD), Meteorological Observatory Lindenberg – Richard Aßmann Observatory, 15848, Tauche OT Lindenberg, Germany
[3]Institute for Geophysics and Meteorology, University of Cologne, 50969 Cologne, Germany

Correspondence: Moritz Löffler (moritz.loeffler@dwd.de)

Abstract.

This study introduces two new retrievals for ground-based microwave radiometers (MWR) and demonstrates that, together, they solve the misrepresentation issue that makes it challenging to assimilate cloudy-sky brightness temperatures. Multiple studies have shown that assimilating MWR brightness temperatures is beneficial to numerical weather prediction, despite rejecting substantial amounts of valid observations from the assimilation due to the presence of liquid water clouds. Cloud detection complemented with a cloud clearing retrieval makes this rejected data available for direct assimilation.

We scrutinize the introduced cloud detection retrieval and cloud clearing retrieval using multiple approaches. For one, we contextualize the new retrievals with reference retrievals. Secondly, we determine the retrieval sensitivity to instrument errors using a Monte Carlo method. And most importantly, we assess the representativeness of the retrieval products, which is crucial for data assimilation, through observation minus background statistics.

Our analysis reveals that the new cloud detection retrieval predicts less false positive cloudy-sky cases ($-13\,\%$ over two years) compared to the established reference. Additionally, the cloud-clearing retrieval improves the representativeness between observation and background to the extent that artificial clear-sky and native clear-sky statistics almost match. Considering the minimal instrumentation required, both retrievals perform surprisingly well for elevation angles from zenith down to $4.8\,°$.

Overall, our findings demonstrate that combining cloud detection and cloud clearing retrievals improves the representativeness between observations and model. This retrieval combination enables the direct assimilation of cloudy-sky brightness temperatures.

https://doi.org/10.5194/egusphere-2026-2264
Preprint. Discussion started: 8 July 2026

1 Introduction

Assimilating remote sensing and in-situ observations improves the representation of the atmosphere in the initial state of numerical weather prediction (**NWP**) models. The atmospheric boundary layer is especially underrepresented in NWP models, and ground-based remote sensing is increasingly considered to improve the representation of the atmospheric boundary layer (e.g., Cimini et al., 2020; Illingworth et al., 2019). In light of this underrepresentation, the US National Research Council et al. (2009) proposed a network of ground-based profilers to improve the representation of the atmospheric boundary layer in NWP models.

Among the available ground-based remote sensing instruments, microwave radiometers (**MWR**) are one of the promising candidates to close the data gap in the atmospheric boundary layer (Vural et al., 2024; Martinet et al., 2020). We use observations from MWR to retrieve temperature and humidity profiles up to $3\,km$ (Cimini et al., 2006) and liquid water path (**LWP**) by inverse radiative transfer modeling. MWR products have already been successfully assimilated by Meteo France (Martinet et al., 2020). After De Angelis et al. (2016) adapted the Radiative Transfer for TIROS Operational Vertical Sounder (**RTTOV**) forward operator for ground-based applications, brightness temperature observations ($\mathbf{T_B}$) have been assimilated directly (Ikuta et al., 2025; Vural et al., 2024; Cao et al., 2023). The rapid development over the past decade has established the potential for assimilating MWR; nevertheless, some questions remain. This study is closely related to two of these questions: how to handle the presence of liquid water clouds and how to assimilate off-zenith observations, which contribute independent information to the temperature profile in the lower troposphere (Turner and Löhnert, 2021) and contain information on horizontal gradients of water vapor (Marke et al., 2020).

One advantage of MWRs is that the presence of clouds does not limit their observation capability (Löhnert et al., 2007). But when assimilating MWR T_Bs in the presence of liquid water clouds, the representativeness between model and MWR T_Bs is significantly reduced (Vural et al., 2024). To account for this, Vural et al. (2024) relied on a cloud detection and inflated the observation error in detected cloudy-sky cases. The observation error is a composite error with contributions from instrument error, error of the observation operator (e.g., radiative transfer model), and error of representativeness (Geer and Bauer, 2011). More recently, Ikuta et al. (2025) successfully circumvented the need to detect clouds before assimilation of MWR T_Bs with a variational quality control (VarQC) (Anderson and Järvinen, 1999) integrated into their assimilation system. The VarQC reduces the weight of observations based on their likelihood of being outliers, without completely rejecting them. Both the inflation of the observation error and the VarQC method selectively decrease the impact of the observation on the initial state of the NWP model (Hunt et al., 2007).

Past studies dealing with MWR have supplied various liquid water cloud detection retrievals for stand-alone MWR tailored to their specific needs: Marke et al. (2016) rely on a threshold of the standard deviation (**STD**) of LWP; Turner (2007) relies on the $30\,min$ STD of T_B at $31\,GHz$; Martinet et al. (2015) supplement the cloud detection of the ceilometer with a threshold for the infra-red (**IR**) brightness temperatures ($\mathbf{T_{B\text{-}IR}}$) observed by an IR-radiometer. This method discriminates ice-clouds from liquid water clouds with the cloud base temperature provided by the IR-radiometer, however partially transparent clouds lead to an underestimation of the cloud base temperature; Hocke et al. (2016) computed cloud cover statistics with a threshold at

https://doi.org/10.5194/egusphere-2026-2264
Preprint. Discussion started: 8 July 2026

3σ of the LWP; De Angelis et al. (2017) rely on a combination of T_{B-IR} and STD of T_B at $31\,GHz$, for a retrieval with high certainty on the clear-sky detection; This combined retrieval was adapted by Vural et al. (2024), obtaining a cloud detection retrieval with a finer time resolution; Finally, Ahn et al. (2015) published a cloud detection retrieval which relies on dynamical thresholds for T_{B-IR} and for the STD of T_{B-IR}. They found it able to detect both ice and liquid water clouds. However, all cloud detection retrievals known to the authors have limitations that make them unattractive for data assimilation. The three main limitations are a low time resolution, a focus on high certainty for clear-sky cases, and limitations in instrumentation and operational procedures, which require time series with a $1\,s$ time resolution and are sufficiently long to compute the STD of LWP or T_Bs. Considering the standard operation procedures agreed on by networks such as ACTRIS [1] and E-PROFILE[2] (Rüfenacht et al., 2021), the cloud detection retrievals are limited to zenith measurements. However, a cloud detection at off-zenith is a prerequisite for assimilating off-zenith MWR T_Bs. Ideally, a cloud detection retrieval is independent of the MWR manufacturer, auxiliary instrumentation, measurement configuration, or elevation angle, and is easily adaptable for new locations, simplifying rollout for large networks.

Despite any cloud detection, the reduced representativeness of the MWR T_B observations in the presence of liquid water clouds remains. This study focuses on the representativeness of MWR T_Bs and ICON-D2, the current operational numerical weather prediction model for an area covering Germany. Similar to space born microwave radiometry (Geer et al., 2012), we attribute the reduced representativeness to the limits in resolving LWP variations below the grid scale (e.g. $2\,km$ ICON-D2), to the difficulties in predicting the exact location of clouds, and to the prediction of less cloud liquid water in the ICON model than observed at German ACTRIS sites (Shuvalova et al., 2023). These circumstances motivate removing the contribution of cloud liquid water to the observed radiances, so that only the signals from thermal emission and the transmission of oxygen (temperature) and water vapor remain.

To address the challenges outlined above, we developed and evaluated two retrievals: a cloud detection retrieval (Cloud-R_{ERA5}) and a cloud clearing retrieval (Clearing-R_{ERA5}). The retrievals rely on neural networks (Sect. 2.4), trained on T_Bs from a radiative transfer model (Sect. 2.3) and from an ECMWF[3] reanalysis data v5 (**ERA5**) climatology (Sect. 2.2). We tested the sensitivity of Cloud-R_{ERA5} to instrument errors with a Monte Carlo method (Sect. 2.5), independently from ERA5 on ICON-D2 T_Bs in Sect. 3.1.1. In Sect. 3.1.2, we compare Cloud-R_{ERA5} to reference cloud detection methods presented in Sect. 2.7. The comparison to reference cloud detections is useful but has limited implications; therefore, the effect of the choice of cloud detection on observation minus background statistics (Sect. 3.1.3) is the decisive test for the suitability of Cloud-R_{ERA5} for data assimilation. In the second half of our results section, we investigate the effectiveness of Clearing-R_{ERA5} in removing the signature of cloud liquid water from MWR T_Bs. To investigate, we compare cleared and interpolated T_Bs in several case studies in Sect. 3.2.1. Thereafter, in Sect. 3.2.2, we analyze the effect of Clearing-R_{ERA5} on the cloudy-sky observation error with observation minus background statistics. We finally discuss and summarize our findings in Sect. 4.

[1]The Aerosol, Clouds and Trace Gases Research Infrastructure; www.actris.eu
[2]EUMETNET program for surface-based profile observations
[3]European centre for midrange weather forecast

https://doi.org/10.5194/egusphere-2026-2264
Preprint. Discussion started: 8 July 2026

2 Methods and Data

Following this general overview and the motivation of our study, we now introduce our methods and data. This includes introducing data from observations (Sect. 2.1), data from atmospheric models (Sect. 2.2), and the radiative transfer model used to calculate the corresponding T_Bs (Sect. 2.3). Thereafter we dive into the retrieval design (Sect. 2.4), how we determined the sensitivity to instrument errors (Sect. 2.5), give an introduction to the observation error and observation minus background statistics (Sect. 2.6) and introduce our reference cloud detection methods thoroughly (Sect. 2.7).

2.1 Observations

This study utilizes the MWR located at the Meteorological Observatory Lindenberg–Richard-Aßmann-Observatory (**MOL–RAO**), Germany, at $126\,m$ above mean sea level. MOL-RAO is also an ACTRIS cloud remote sensing (**CloudNet**, Illingworth et al. (2007)) site with CloudNet products available since 2004. Furthermore, the Field Experiment on Submesoscale Spatio-Temporal Variability in Lindenberg (**FESSTVaL**, Hohenegger et al. (2023)) was conducted at MOL-RAO between May and September 2021.

The MWR, which we primarily use in this study (DWDHAT), is a HATPRO-G5[4] (Rose et al., 2005) manufactured by Radiometer Physics GmbH (**RPG**). MWRs observe downwelling microwave radiation and primarily record it as T_Bs. The 14 microwave channels of the HATPRO-G5 are evenly distributed between the K- and V-band, as shown in Table 1. The instrument is equipped with a zenith-pointing IR-radiometer with one channel at $\lambda = 1.5 * 10^{-6}\,m = 1.5\,\mu m$. In the given measurement configuration, the MWR observes the zenith with a $1\,s$ resolution and a $1\,s$ integration time. The continuous observations are interrupted by elevation scans every $20\,min$. The elevation scans provide one observation of the 14 T_B for each of the 10 elevation angles listed in Table 2 with a $10\,s$ integration time. In this study, we use MWR T_Bs from May 2021 – April 2023 (Knist and Görsdorf, 2026).

During the FESSTVaL campaign, T_B observations and retrieved LWP were available from a second HATPRO-G5 referred to as FOGHAT (Löhnert et al., 2022). FOGHAT was located on the platform directly next to DWDHAT. The LWP retrieval applied to the T_B observations of both HATPRO-G5 at MOL-RAO during the FESSTVaL campaign is a multilinear regression (Löhnert and Crewell, 2003) trained on a climatology of radiosondes from MOL-RAO. We refer to this LWP retrieval as LWP-R_{RS}. Both sets of LWP serve as independent references for the new cloud detection retrieval evaluated in this study.

Band	K-Band							V-Band						
Frequency in GHz	22.24	23.04	23.84	25.44	26.24	27.84	31.40	51.26	52.28	53.86	54.94	56.66	57.30	58.00

Table 1. Channel center frequencies of the 14 microwave channels of the MWR system used in this study.

[4]Humidity And Temperature PROfiler

https://doi.org/10.5194/egusphere-2026-2264
Preprint. Discussion started: 8 July 2026

Elevation in °	90.0	30.0	19.2	14.4	11.4	8.4	6.6	5.4	4.8	4.2

Table 2. Elevation angles at which the MWR performs the boundary layer scans in our setup.

Rain, a degraded radome, and calibration issues introduce uncertainty and may lead to T_B-biases. The piezoelectric precipitation sensor (Salmi et al., 2005) flags data affected by rain. This precipitation sensor is included in the WXT536 weather station, which is integrated into the MWR setup. We identified a wet or degraded radome with the toolbox published by Löffler (2024). A degraded radome will lead to biased T_Bs after rain events, which the precipitation sensor does not flag (Böck et al., 2025). The 20-month dataset contains one particularly large gap from 26 August 2021 to 18 January 2022, due to radome degradation, an instrument failure, and subsequently a calibration issue. Carefully flagged data are removed from our analysis.

2.2 Atmospheric Models

Atmospheric models are a valuable addition to observations because they are consistent and stable over longer and sometimes even climatologically representative time periods. This section introduces the operational NWP model and the reanalysis dataset used in this study. The atmospheric reanalysis dataset serves as a climatologically representative reference to train the MWR retrievals evaluated in this study. The NWP model is used for O-B statistics to quantify the suitability of the MWR T_Bs for data assimilation and as an independent reference to evaluate the MWR retrievals.

ERA5 is the fifth ECMWF reanalysis dataset (Hersbach et al., 2023). Like other reanalysis datasets, ERA5 unifies many historical observations to obtain a full record of the global atmosphere. It is available from 1940 to the present. The ERA5 dataset has a horizontal resolution of 0.02 °, which is equivalent to $\sim 30\,km$ at MOL-RAO. It is available on 37 pressure levels ranging from $1\,hpa$ to $1000\,hpa$. For reasons of numerical stability, we limited the maximum profile height to $30\,km$. Below $30\,km$ the pressure levels are evenly spaced with a resolution of $25\,hpa$. The ERA5 pressure levels do not include data at the surface level. We use a dataset from the ERA5 model column closest to MOL-RAO, from January 2010 to December 2021, to train, validate, and test the retrievals.

The ICON-D2 is the operational NWP model at DWD since March 2020 for high-resolution $48\,h$ forecast in Germany and neighboring countries. ICON-D2 builds on the ICOsahedral Non-hydrostatic (**ICON**) modeling framework (Zängl et al., 2015). The ICON-D2 dataset has a horizontal resolution of $\sim 2.1\,km$ at MOL-RAO. The ICON-D2 backgrounds are available at each full hour. ICON-D2 is defined on 65 model levels ranging between $10\,m$ above ground and $22\,km$ above mean sea level with a vertical resolution between $20\,m$ near ground and $2600\,m$ at the top of the atmosphere. The height of the surface level of the grid cell closest to MOL-RAO is $76\,m$ above mean sea level. We extend the ICON-D2 backgrounds to $30\,km$ altitude with midlatitude standard atmospheres, summer or winter, respectively. We use two years of ICON-D2 backgrounds to validate the retrievals against an independent model reference and for Monte Carlo simulations.

https://doi.org/10.5194/egusphere-2026-2264
Preprint. Discussion started: 8 July 2026

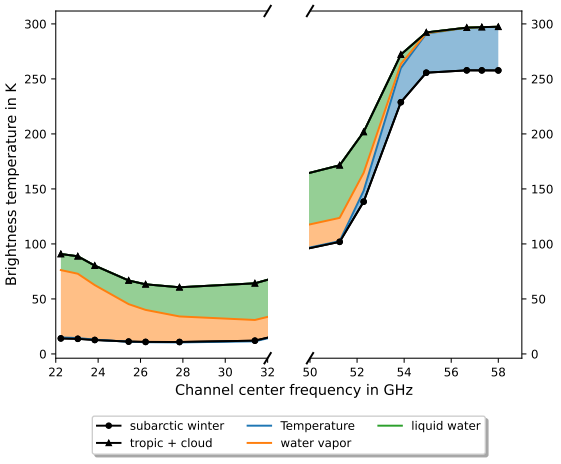

Figure 1. Brightness temperature spectrum of subarctic winter (clear sky) and tropic (cloudy sky). Contributions by stepwise adapting temperature (blue) and water vapor (orange) and finally adding a liquid cloud (green). These spectra were calculated with lbl_rt_py (Löffler et al., 2025) in the configuration described in Sect. 2.3.

2.3 Radiative transfer model and absorption models

We require a radiative transfer model to compute the T_Bs from the predicted model profiles of pressure, temperature, humidity, and liquid water content.

The radiative transfer model used in this study (lbl_rt_py, Löffler et al., 2025) builds on the line-by-line absorption coefficients for water vapor, oxygen (o2_abs19.f), and nitrogen published by Rosenkranz (2022) and on Simmer (1994, p. 82 ff). The radiative transfer model calculates the liquid water absorption according to Ellison (2007), and the air mass correction for off-zenith observations according to Levis et al. (2010, p. 121) with the "best average" refractive coefficients from Rüeger (2002).

We compute the T_B equivalents of the ERA5 and the ICON-D2 model columns with lbl_rt_py in the above-mentioned configuration at the 14 HATPRO frequencies (Table 1). The T_Bs for off-zenith observations are computed from the vertical model column only, thus inferring a horizontally homogeneous atmosphere. The elevation angles considered for this study are given in Table 2. The radiative transfer calculations do not account for the beam width and the bandwidth of the observing channels.

2.4 Retrieval design

The central elements of the new retrievals presented in this study are neural networks trained on T_Bs simulated from the ERA5 climatology with lbl_rt_py (Sect. 2.3). In the following, we describe the training of the neural networks within these retrievals, as well as their structure and interactions.

The two new retrievals in this study predict the presence of clouds (Cloud-R_{ERA5}) and the theoretical clear-sky T_B equivalents (Clearing-R_{ERA5}). In more general terms, the two retrievals are essentially designed to detect and remove the contribution

https://doi.org/10.5194/egusphere-2026-2264
Preprint. Discussion started: 8 July 2026

from cloud liquid water to the T_B-spectrum (see Fig. 1). Table 3 provides the retrievals with input, output, and resolution. We extracted the input and the desired output of the retrievals from the ERA5 model for training and hyperparameter optimization.

All retrievals rely on neural networks implemented within the scikit-learn (Pedregosa et al., 2011) Python library, namely `MLPClassifier` and `MLPRegressor`. We chose these multi-layer perceptron (**MLP**) models because they are stable, well-tested, and easily accessible, and therefore ideal for rapid prototyping and establishing the baseline performance. Given the moderate dimensionality of the T_B vectors and the smooth nonlinear relationships involved, a feed-forward MLP is sufficient for our purposes.

During neural-network optimization, it proved essential to standardize the inputs to unit variance using `sklearn.preprocessing.StandardScaler`. We tested dimensionality reduction but ultimately abandoned it because it degraded retrieval performance.

For model training and selection, the ERA5 dataset was chronologically split into training (9 years), validation (2 years), and test (1 year) sets. We trained multiple similar neural networks with varying combinations of model hyperparameters, such as solver, learning rate, number, and size of hidden layers for each retrieval. We then selected the best neural network manually based on its performance on the validation dataset, and verified its performance on the test dataset.

Retrieval Name	Input	Output	Resolution
Cloud-R_{ERA5}	T_Bs at 14 MW-frequencies (Table 1), $sin(DOY)$, $cos(DOY)$, $sin(HOD)$, $cos(HOD)$	binary: presence of liquid water clouds (threshold$_{LWP} = 5\,g\,m^{-2}$)	$10\,s$
Clearing-R_{ERA5}	T_Bs at 14 MW-frequencies (Table 1), $sin(DOY)$, $cos(DOY)$, $sin(HOD)$, $cos(HOD)$	clear-sky T_Bs at 14 MW-frequencies (Table 1)	$10\,s$

Table 3. Input, output, and resolution of the retrievals investigated in this study. We computed the clear-sky T_Bs for ERA5 and ICON-D2 by setting the model cloud liquid water content to zero before the radiative transfer calculation. Some retrievals require the input of day of year (DOY) and hour of day (HOD).

To reduce sensitivity to calibration errors and other instrument errors, Cloud-R_{ERA5} has an internal bias correction of the T_B input. The internal bias correction is performed with an additional neural network. The bias correction counteracts slow-changing errors ($\Delta_t = 24\,h$). To address the high noise levels, the output Cloud-R_{ERA5} is smoothed with a $10\,s$-binned median.

Similar to LWP retrievals (e.g., Crewell and Löhnert, 2003), Clearing-R_{ERA5} exhibits non-zero differences to the unchanged observations during clear-sky episodes. These differences between native and artificial clear-sky T_Bs should ideally be zero when Cloud-R_{ERA5} does not detect clouds. The retrieval corrects non-zero differences by subtracting the $24\,h$ mean clear-sky difference from Clearing-R_{ERA5}'s output. Cloud-R_{ERA5} detects the clear-sky cases for this correction. This correction is averaged in $24\,h$ bins and forward propagated if the next bin has no clear-sky cases.

https://doi.org/10.5194/egusphere-2026-2264
Preprint. Discussion started: 8 July 2026

2.5 Retrieval error and sensitivity to instrument errors

Determining the error and the sensitivity to instrument errors of the two new retrievals is one of the central aims of this study. When using the retrieval products, the error of the provided product is relevant. This product error is the sum of the retrieval error and the retrieval's response to a given instrument error. We introduce our methodology in the following.

MWR observations will always be subject to instrument errors, which vary on different time scales. Böck et al. (2025) discuss the mechanisms that lead to errors in the observed T_Bs and the resulting characteristics of the errors. The neural networks' responses to instrument errors are not necessarily linear or even continuous. E.g. Szegedy (2013) found that deep neural networks can be very sensitive to small perturbations of the input data. When evaluating the performance of retrievals for MWRs, it is therefore essential to account for these possible instrument errors and evaluate their effect on the retrieval products.

In addition to these instrument errors, the retrievals themselves will also always introduce random and systematic errors into the products that they provide. Both systematic and random errors can result from errors in the radiative transfer calculations, e.g., absorption model uncertainties, and mismatches in the model climatology, e.g., due to model orography or instruments placed on buildings. Even with perfect training data, retrieval errors would also result from the model architecture, which cannot fully describe all processes, and even more in our case, the inversion of the radiative transfer calculation is underdetermined.

We approximate the combined product error with different approaches. For the cloud detection (Cloud-R_{ERA5}) we rely on a Monte Carlo method (Sect. 3.1.1) and we compare Cloud-R_{ERA5} to other cloud detection retrievals introduced in Sect. 2.7 (Sect. 3.1.2). For the cloud clearing retrieval Clearing-R_{ERA5} we rely on comparisons to interpolated observations (Sect. 3.2.1) and observation minus background statistics with ICON-D2 (Sect. 3.2.2).

2.6 Observation error and observation minus background statistics

This study analyzes observation minus background (**O-B**) statistics. O–B statistics provide valuable insights into the magnitude and structure of differences between observations and model backgrounds. These differences arise from a combination of observation errors and forecast errors. Observation errors reduce the weight assigned to an observation in the data assimilation process, whereas forecast errors are linked to the potential value of observations for numerical weather prediction.

Following Geer and Bauer (2011), we use the sample standard deviation of O–B to approximate the random component of the observation error. The observation error consists of the instrument error, the error of the observation operator (e.g., radiative transfer model), and the error of representativeness. Generally some forecast errors are difficult to separate from representativeness errors, therefore also forecast errors – such as mislocation errors – contribute to O–B statistics. Geer and Bauer (2011) include forecast errors into the observation error making it more practical to approximate.

Selected contributions to the instrument error from Böck et al. (2025) and Böck et al. (2024) are as follows: Calibration uncertainties of up to $\Delta T_B = 1\,K$ and noise levels of up to $\sigma_{T_B} = 0.32\,K$; Instrument-specific errors, e.g. due to bandpass shape, gain errors and shifts of the actual frequency with respect to the specified frequency have lead to $\Delta T_B = 0.6\,K$. Uncertainties of the elevation angle and an instrument tilt lead to large biases at low elevations in the K-band of up to $\Delta T_B \simeq 10\,K/0.6°$.

https://doi.org/10.5194/egusphere-2026-2264
Preprint. Discussion started: 8 July 2026

Lastly, also external sources, such as water on the radome, radio frequency interference, and ground pickup from side lobes, introduce errors in the observed brightness temperatures.

Contributions to the error of the radiative transfer model are the following: Uncertainties of the optical parameters lead to errors up to $\Delta T_B = 3.3\,K$ (Cimini et al., 2018) for the line-by-line absorption coefficients from Rosenkranz 2017; Lacking bandpass shape and beamwidth can lead to errors up to $\Delta T_B = 1.5\,K$ (Meunier et al., 2013); Simplifications like a flat earth or missing refraction will lead to errors in the optical thickness and $\Delta T_B \leq 6.1\,K$ (Meunier et al., 2013).

Contributions to the error of representativeness include the observation of structures that model grids cannot resolve, e.g., LWP variations within clouds (Geer and Bauer, 2011), Mismatch of the orography and therefore of observed and modeled atmospheric column in complex terrain, or if instruments are on buildings, and mismatch of the location due to missing or imprecise beam tracing.

2.7 Reference cloud detection retrievals

This section provides a detailed introduction to the cloud detection retrievals used as references for Cloud-R$_{ERA5}$ and explains the recall matrices used to compare them. This study provides three reference cloud detection retrievals, STD30, STD6, and LWP-R$_{RS}$. STD6 is an adaptation of STD30 which was first mentioned by De Angelis et al. (2017) and LWP-R$_{RS}$ is an LWP retrieval combined with a threshold.

STD30 (De Angelis et al., 2017) provides a high certainty in detecting clear-sky scenes. In STD30, a clear-sky scene must fulfill both of the following criteria: The observed T$_{B-IR}$ must be smaller than $243.7\,K$ ($-30\,°C$) and the $30\,min$ rolling STD of T$_B$ at $31.4\,GHz$ must be smaller than $0.5\,K$. By design, this method will flag observations $15\,min$ before the beginning and after the end of a cloudy-sky observation as cloudy. The large temporal uncertainty of STD30 motivated changes to reduce this uncertainty.

Vural et al. (2024) introduced STD6 as an adaptation from STD30. The rolling time window for calculating the STD of T$_B$s at $31.4\,GHz$ is reduced to $6\,min$ with a new threshold of $0.25\,K$. The threshold for T$_{B-IR}$ is the same as in STD30. STD6 provides a reduced fraction of false positive cloud detections before and after cloudy-sky observations, thereby increasing the fraction of clear-sky observations.

Both STD30 and STD6 are limited to zenith observations for two reasons. Firstly, the retrievals rely on an IR-radiometer. Of those MWRs equipped with an IR-radiometer, most have a fixed zenith-pointing IR-radiometer, and only the newest HATPRO-G5 instruments optionally include an IR-radiometer that follows the MWR's elevation scan. Therefore, the T$_{B-IR}$ observation is missing for off-zenith observations. Secondly, STD30 and STD6 rely on sufficiently long ($30\,min$ and $6\,min$) time series of T$_B$s with $1\,s$ time resolution. In the typical measurement configuration, such time series are only available for the zenith-pointing observations. Therefore, STD30 and STD6 are not suitable for off-zenith observations.

LWP-R$_{RS}$ is the third reference cloud detection retrieval in this study. The LWP retrieval, LWP-R$_{RS}$ (Löhnert et al., 2007), was used to compute the LWP in the FESSTVaL dataset. In combination with a $5\,g\,m^{-2}$ threshold, LWP-R$_{RS}$ also provides the binary information clear-sky/cloudy-sky. The FESSTVaL LWP dataset is published only for zenith observations, limiting cloud detection with LWP-R$_{RS}$ to zenith angles.

https://doi.org/10.5194/egusphere-2026-2264
Preprint. Discussion started: 8 July 2026

		Prediction	
"True" reference		TNR	FAR
		FNR	POD

Table 4. All recall matrices in this study are structured as indicated by this table. With TNR: true negative rate; FNR: false negative rate; FAR: false alarm rate; POD: probability of detection. Clear and cloudy are indicated by the symbols and respectively.

We mainly compare the predictions of the different cloud detection retrievals using recall matrices (see Table 4). The titles of the rows of the recall matrices (left) contain the "true" reference, and the titles of the columns (top) contain the predictor. A recall matrix contains true negative rate (**TNR**), false negative rate (**FNR**), false alarm rate (**FAR**), and probability of detection (**POD**). These performance metrics are defined by

$$TNR = \frac{TN}{TN+FP} \qquad FNR = \frac{FN}{TP+FN} \qquad FAR = \frac{FP}{TN+FP} \qquad POD = \frac{TP}{TP+FN} \tag{1}$$

with the confusion matrix components true negative (TN), false negative (FN), true positive (TP), and false positive (FP).

3 Results

In the following, we analyze the performance of the novel multi-angle neural-network-based cloud detection (Cloud-R$_{ERA5}$) and cloud-clearing (Clearing-R$_{ERA5}$) retrievals. We begin by examining the performance of Cloud-R$_{ERA5}$ (Sect. 3.1), which we designed to detect liquid water clouds at zenith and off-zenith angles for our O-B statistics. Thereafter, in Sect. 3.2, we demonstrate that the Clearing-R$_{ERA5}$ conceptually works and we quantify its impact on the approximated observation error.

Technically speaking, there are separate cloud detection and cloud clearing retrievals for each elevation angle. However, the only difference between retrievals for different elevation angles is the elevation angle used to compute the T$_B$s from the ERA5 model columns. We therefore use the singular (e.g., cloud detection retrieval) for easier reading and to avoid confusion.

All retrievals performed well on the test and validation subset of the ERA5 T$_B$ data. The following evaluations of the retrievals in this study were performed independently of ERA5 on observed T$_B$s and T$_B$s simulated from ICON-D2 backgrounds.

3.1 Cloud detection

This study employs three different approaches to evaluate the potential and the limitations of Cloud-R$_{ERA5}$. In Sec. 3.1.1, we use a Monte Carlo analysis to derive Cloud-R$_{ERA5}$'s retrieval sensitivity to instrument errors. In Sec. 3.1.2, we evaluate the agreement between Cloud-R$_{ERA5}$ and other observation-based liquid cloud detections. In Sec. 3.1.3, we compare the effects of cloud detection with Cloud-R$_{ERA5}$ and STD30 on O-B statistics.

One central question when developing Cloud-R$_{ERA5}$ was the choice of a general detection limit for liquid clouds. On the one hand, a lower threshold led to worse performance metrics, particularly the false alarm rate (FAR). On the other hand, the

https://doi.org/10.5194/egusphere-2026-2264
Preprint. Discussion started: 8 July 2026

		Cloud-R$_{ERA5}$					
		90°		30° to 11°		8° to 4°	
LWP$_{ICON-D2}$							
		0.76 - 0.98	0.02 - 0.23	0.60 - 0.99	0.01 - 0.40	0.57 - 0.98	0.02 - 0.43
		0.01 - 0.08	0.92 - 0.99	0.00 - 0.09	0.91 - 1.00	0.00 - 0.07	0.93 - 1.00

Table 5. 95 % confidence intervals from Monte Carlo method of recall matrix for Cloud-R$_{ERA5}$, which includes bias correction with Bias-R$_{ERA5}$. Results obtained from randomly biased T$_B$s, calculated from ICON-D2 backgrounds, by Cloud-R$_{ERA5}$. We computed the reference cloud detection from the ICON-D2 cloud liquid water and a threshold, i.e., $LWP_{ICON-D2} > 5\,gm^{-2}$. "30° to 11°" includes 30°, 19.2°, 14.4° and 11.4°. "8° to 4°" includes 8.4°, 6.6°, 5.4°, 4.8° and 4.2°.

threshold should be as low as possible to increase the probability of detection (POD). To determine the ideal threshold, we required that the impact of the chosen threshold LWP on the observed T$_B$s is less than both the instrument error and the clear-sky observation error approximated with O-B statistics. All this taken into account, we fixed the threshold at $LWP = 5\,gm^{-2}$ to balance the two competing metrics, FAR and POD.

3.1.1 Cloud-R$_{ERA5}$'s sensitivity to instrument errors

We generally expect that instrument errors will occur. Instrument errors alter the retrieval output, and the retrieval's sensitivity to instrument errors determines the magnitude of this change. This section examines the outcomes of Monte Carlo simulations applied to the cloud detection with Cloud-R$_{ERA5}$ from two perspectives. First, we discuss the confidence intervals in the recall matrices (Table 5). Second, we analyze the shape of the binned cloud detection rate (POD$_{\text{local}}$) and its implications. However, before presenting the first results, we now introduce the Monte Carlo method used to assess the retrieval sensitivity to instrument errors.

We determined the retrieval sensitivity to instrument errors by adding static biases using a Monte Carlo method. We perturbed the ICON-D2 T$_B$ equivalents 100 times by adding a static random Gaussian T$_B$ bias with $\sigma_{bias} = 0.5\,K$. The T$_B$s of each channel were perturbed independently 50 times, simulating a channel-dependent static bias. Fifty other times, we perturbed T$_B$s of the K-band and V-band independently, simulating a band-dependent static bias. The band-dependent bias is identical for channels within the K-band or the V-band; however, it is uncorrelated between the K-band and the V-band. In this study, we frequently refer to the retrieval sensitivity to instrument errors to denote the ability of the retrievals to produce correct results in the presence of biased input T$_B$s.

The confidence intervals in the recall matrices (Table 5) show the overall performance of Cloud-R$_{ERA5}$ under adverse conditions. Given the adverse conditions induced by T$_B$ biases with $\sigma_{bias} = 0.5K$, POD is greater than 91 % for all elevations

https://doi.org/10.5194/egusphere-2026-2264
Preprint. Discussion started: 8 July 2026

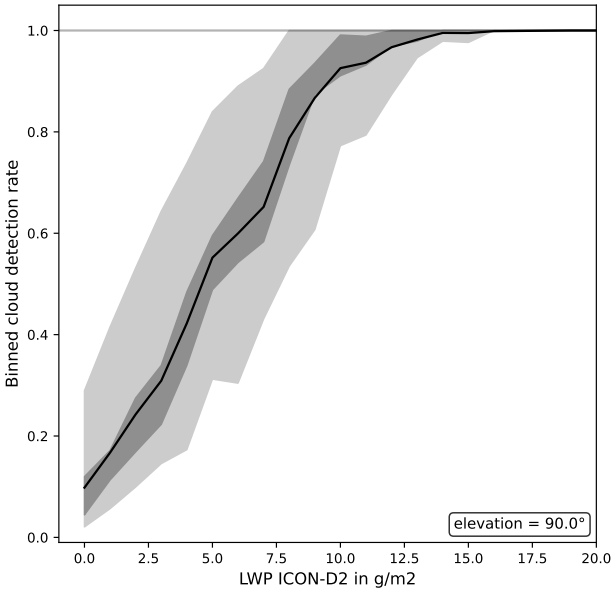

Figure 2. Binned cloud detection rates (eq. 2, $\text{POD}_{\text{local}}$) of Cloud-$\text{R}_{ERA5}$ tested on 2 years of ICON-D2 backgrounds. The LWP (x-axis) is the integrated cloud liquid water content of the ICON-D2 backgrounds. The dark shading indicates the 25th and 75th percentiles, the light shading indicates the 5th and 95th percentiles. The percentiles are determined by biasing the input T_Bs with a Monte Carlo method. The plot shows only the zenith cloud detection.

and $97.3\,\%$ on average. These high PODs come at the cost of fairly high FARs of up to $43\,\%$ and $10.9\,\%$ on average. Looking more specifically at zenith, Table 5 reveals only slight differences of POD to the other elevations, while at the same time, the maximum expected FAR is $23\,\%$, which is significantly lower ($-47\,\%$) than the off-zenith FAR. This significant difference in the maximum FAR is the main difference between zenith and off-zenith Cloud-R_{ERA5} recall matrices. These results show that while the false alarm rate can be substantial for some constellations of the T_B biases, Cloud-R_{ERA5} confidently predicts liquid water clouds under adverse conditions. To obtain a better procedural understanding for all elevations and to explain the differences in FAR, we will analyze $\text{POD}_{\text{local}}$, which is introduced in the following paragraph.

Binning cloud detection rates in [LWP$-1\,gm^{-2}$, LWP] yields $\text{POD}_{\text{local}}$ as a function of LWP. $\text{POD}_{\text{local}}$ illustrates how Cloud-R_{ERA5} responds in the presence of clouds and how the total mean POD accrues. The $\text{POD}_{\text{local}}$ is defined by

$$\text{POD}_{\text{local}}(LWP_i) := \frac{\text{D}(LWP_i)}{\text{N}(LWP_i)} \tag{2}$$

where the $\text{D(LWP}_i\text{)}$ are detections per bin and $\text{N(LWP}_i\text{)}$ are the number of samples per LWP-bin. Next, we look into $\text{POD}_{\text{local}}$'s shape and response to instrument errors, first for zenith then for off-zenith.

Zenith $\text{POD}_{\text{local}}$ (Fig. 2) increases steadily following an S-shaped curve similar to a logistic function. In the transition, for $LWP \in [0\,gm^{-2}, 10\,gm^{-2}]$, $\text{POD}_{\text{local}}$ visualizes the uncertainty of Cloud-R_{ERA5} and how FAR and POD depend on the choice of the LWP-threshold. Thereafter, $\text{POD}_{\text{local}}$ surpasses $90\,\%$ at $LWP = 11 \pm 2\,gm^{-2}$ and reaches $100\,\%$ for $LWP \gtrsim$

https://doi.org/10.5194/egusphere-2026-2264
Preprint. Discussion started: 8 July 2026

		STD30		STD6		LWP - R_{RS}	
Cloud -R_{ERA5}	☀	0.54	0.46	0.70	0.30	0.94	0.06
	☁	0.07	0.93	0.10	0.90	0.20	0.80

Cloud cover	STD30	Cloud R_{ERA5}	STD6	Cloud R_{ERA5}	LWP R_{RS}	Cloud R_{ERA5}
	0.71	0.51	0.60	0.51	0.44	0.52

Table 6. Recall matrices and cloud cover determined by zenith cloud detection retrievals. Results from Cloud-R_{ERA5} are compared to other reference cloud detection schemes. It is important to note that, technically speaking, Cloud-R_{ERA5} is the "True" reference for the other cloud detection schemes in these recall matrices. STD30 and STD6 are the 30-minute and 6-minute STD of the 31 GHz channel combined with an IR-radiometer (see Sect. 2.7). The LWP-based cloud detection uses a detection limit of $LWP = 5\,g\,m^{-2}$.

$15\,g\,m^{-2}$, thereby underlining the reliable detection of clouds with increasingly relevant amounts of liquid water. These findings show — and this is consistent for elevation angles $\geq 4.8°$ (Fig. A1) — how Cloud-R_{ERA5} transitions from clear-sky to cloudy-sky detection, and that beyond this transition, cloud detection is perfect.

The off-zenith POD_{local} (Fig. A1) provide insights into differences and similarities of Cloud-R_{ERA5} at different elevation angles. In particular, the sensitivity to instrument errors varies with elevation angle, while the shape of the curve remains similar. The off-zenith POD_{local}s explain why Cloud-R_{ERA5}'s FAR is more sensitive to instrument errors than the POD: All of the cases with true clear-sky ($LWP_{ICON} < 5\,g\,m^{-2}$) are within the LWP-range with pronounced sensitivity to instrument errors. However, for true cloudy-sky cases ($LWP_{ICON} \geq 5\,g\,m^{-2}$), Cloud-$R_{ERA5}$'s sensitivity to instrument errors is limited to low LWPs.

Summarizing the results from the Monte Carlo analysis, we find that Cloud-R_{ERA5} detects liquid water clouds at all elevation angles, even when faced with adversely biased brightness temperatures. In the following section, we continue to investigate the performance of Cloud-R_{ERA5} by comparing established reference cloud detections to Cloud-R_{ERA5}'s predictions from real observations rather than modeled T_Bs.

3.1.2 Comparing Cloud-R_{ERA5} to reference cloud detections

In the following, we compare Cloud-R_{ERA5} with reference cloud detection retrievals to better understand its advantages and shortcomings. These quantitative comparisons (Table 6) rely on data from FESSTVaL during summer 2021. Some of the differences become particularly pronounced during summer due to the relatively more frequent occurrence of cumuliform clouds and the relatively less frequent occurrence of stratiform clouds. We use Cloud-R_{ERA5} as the shared reference to compare all other cloud detection schemes; the full recall matrix is shown in Table A1.

https://doi.org/10.5194/egusphere-2026-2264
Preprint. Discussion started: 8 July 2026

We begin by comparing Cloud-R$_{ERA5}$ to the established cloud detection retrieval STD30 and to STD6. Table 6 shows, that STD30 (STD6) detects more clouds overall than Cloud-R$_{ERA5}$.

With Cloud-R$_{ERA5}$ as a reference, STD30 and STD6 detect $93\,\%$ and $90\,\%$ of the cloudy-sky cases respectively. However, they miss a substantial fraction of the clear-sky cases identified by Cloud-R$_{ERA5}$, namely $46\,\%$ for STD30 and $30\,\%$ for STD6. This indicates a pronounced tendency toward false cloud detections, particularly for STD30.

When switching the perspective with STD30 or STD6 as "true" reference, Cloud-R$_{ERA5}$ misses $32\,\%$ (STD30) and $24\,\%$ (STD6) of their cloudy-sky detections (Table A1). We determine if this apparent under-detection of clouds by Cloud-R$_{ERA5}$ increases the observation error in Sect. 3.1.3.

We identified two main reasons for STD6 and STD30 detecting more clouds than Cloud-R$_{ERA5}$. First, the coarser time resolutions ($30\,min$ and $6\,min$) extend the detection of a cloud beyond the underlying presence of a liquid water cloud. Cloud-R$_{ERA5}$ on the other hand, with a $10\,s$ resolution, resolves transitions between cloudy-sky and clear-sky more accurately. Second, high water vapor concentrations can increase the clear-sky T$_{B-IR}$ and the STD of T$_{B-31.4GHz}$, necessitating a dynamical threshold for the two variables (Ahn et al., 2015). Both effects are shortcomings of STD30 and STD6, which lead to higher false alarm rates in summer.

Next, we compare Cloud-R$_{ERA5}$ to a cloud detection retrieval based on the LWP timeseries from Löhnert et al. (2022) (LWP-R$_{RS}$) with a threshold of $LWP = 5\,g\,m^{-2}$. LWP-R$_{RS}$ determines a lower cloud cover ($44\,\%$) than Cloud-R$_{ERA5}$ ($52\,\%$). These different cloud covers align with the asymmetry between POD ($80\,\%$) and TNR ($94\,\%$) of LWP-R$_{RS}$ with respect to Cloud-R$_{ERA5}$ (Table 6). The lower cloud cover determined by LWP-R$_{RS}$ indicates that the effective detection limit of Cloud-R$_{ERA5}$ for liquid water clouds is lower than $LWP = 5\,g\,m^{-2}$.

The full comparison of all cloud detections available in this study (Table A1) allows many other interesting considerations. We want to highlight the performance of the main references to Cloud-R$_{ERA5}$, i.e., STD6 and STD30. Both STD6 and STD30 have a POD near $100\,\%$ with respect to LWP-R$_{RS}$. On the other hand, STD6 (STD30) has a FAR of up to $30\,\%$ ($48\,\%$) with respect to LWP-R$_{RS}$. These numbers show the improvement in reducing the FAR from STD30 to STD6. Despite this improvement, the FAR remains high even for STD6, thereby reducing the possible impact of MWR-T$_B$ observations on data assimilation.

The comparisons above of Cloud-R$_{ERA5}$ with reference cloud detection retrievals reveal significant differences. These differences mostly favor Cloud-R$_{ERA5}$, but we cannot rule out adverse effects on the representativeness between observation and model by merely comparing the different retrievals. Therefore, we compare the observations minus background statistics after cloud detection using Cloud-R$_{ERA5}$ and STD30 in the following section.

3.1.3 Impact on observation minus background statistics

We use Observation minus background statistics to approximate the observation error. O-B statistics are therefore relevant for assessing the suitability of observations for data assimilation (Sec. 2.6). The statistics discussed here are based on 20 months of data from May 2021 – April 2023 and are used to compare the impact of the two cloud detection methods Cloud-R$_{ERA5}$ and STD30.

https://doi.org/10.5194/egusphere-2026-2264
Preprint. Discussion started: 8 July 2026

		STD30	
Cloud -R_{ERA5}		0.78	0.22
		0.10	0.90

		Cloud -R_{ERA5}	
STD30		0.89	0.11
		0.20	0.80

Cloud cover	STD30	Cloud R_{ERA5}
	0.56	0.49

Table 7. Recall matrices and cloud cover determined by STD30 and Cloud-R_{ERA5} using 20 months of data from May 2021 – April 2023.

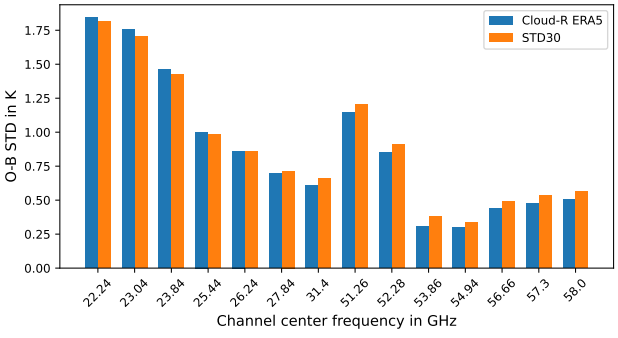

Figure 3. Observation minus background standard deviations for **clear-sky** observations determined by Cloud-R_{ERA5} (blue) by STD30 (orange) for 20 months from May 2021 – April 2023.

For this analysis, we excluded cases with rain, the period 26 August 2021 – 18 January 2022, because of radome degradation, instrument failure, and subsequent calibration issues, and all cases in which the observations were classified as clear-sky while the model indicated cloudy conditions ($LWP_{ICON-D2} \geq 5\,g\,m^{-2}$).

Cloud-R_{ERA5} and STD30 agree on the cloud classification in 84% of all observations, while STD30 diagnoses a larger cloud cover than Cloud-R_{ERA5} (0.56 versus 0.49; Table 7). Thus, the two methods differ noticeably in the number of scenes retained as clear sky. Nevertheless, their impact on clear-sky O-B statistics is very small. Figure 3 shows that the clear-sky O-B

https://doi.org/10.5194/egusphere-2026-2264
Preprint. Discussion started: 8 July 2026

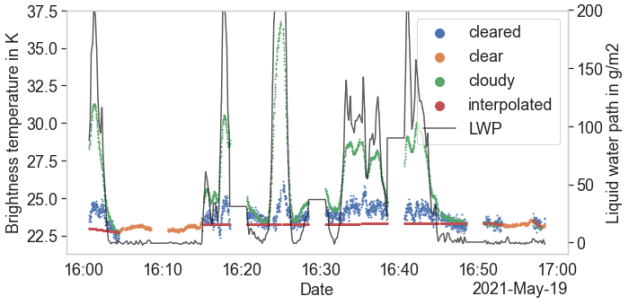

Figure 4. Observed T_B at $23.83\,GHz$ (green: cloudy, orange: clear) during passage of convective clouds. Red: Interpolated T_B between detected clear-sky episodes; Blue: T_B artificially cleared with Clearing-R_{ERA5}. Black: liquid water path. Elevation scans interrupted the zenith observations.

STD obtained with Cloud-R_{ERA5} differs from that obtained with STD30 by only $-0.03\,K$ to $+0.02\,K$ (relative differences between $-9\,\%$ and $+3\,\%$). Even during the summer months of FESSTVaL, when convective clouds are more frequent, the differences remain small, ranging from $-0.06\,K$ to $+0.05\,K$ (relative differences between $-19\,\%$ and $+3\,\%$).

These differences are negligible compared with the increase in O-B STD under cloudy conditions in channels affected by liquid water, where the cloudy-sky STD exceeds the native clear-sky STD by $100\,\%$ to $1500\,\%$ (Table A2). We therefore conclude that, although STD30 and Cloud-R_{ERA5} do not identify exactly the same scenes as cloudy, both retrievals define a clear-sky subset that yields essentially identical O-B statistics. For the following analysis, this means that the choice between the two cloud detection methods has only a minor impact on the approximated clear-sky observation error.

3.2 Cloud clearing

In this second half of the results section, we explore removing the spectral contribution of cloud liquid water (see Fig. 1 from the observed T_Bs from two perspectives. First, in Sec. 3.2.1, we analyze several cases of convective cloud passage to demonstrate that Clearing-R_{ERA5} performs as intended with real observations. Second, in Sect. 3.2.2, we quantify the effect of cloud clearing with Clearing-R_{ERA5} on the approximation of the observation error.

3.2.1 Aggregated case studies

This section evaluates Clearing-R_{ERA5} for observed passages of non-precipitating convective clouds. The aim is to test whether Clearing-R_{ERA5} yields plausible T_Bs when applied to real observations. For this purpose, the cleared T_Bs are compared with linearly interpolated T_Bs between the last clear-sky observation before and the first clear-sky observation after each cloud passage (Eq. (3), Fig. 4). This comparison assumes that changes in temperature and humidity during the cloud passage are small, such that the interpolated T_B provides a suitable reference.

https://doi.org/10.5194/egusphere-2026-2264
Preprint. Discussion started: 8 July 2026

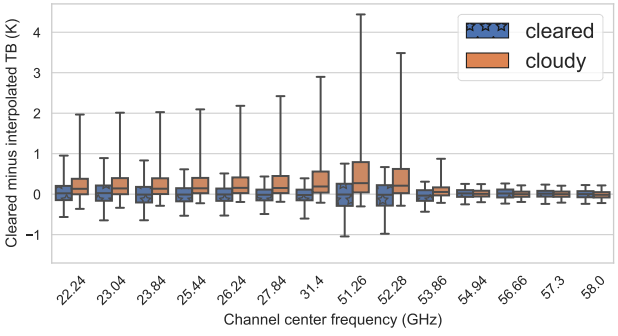

Figure 5. Channelwise statistics of cleared/cloudy observations minus interpolated observations (see Fig. 4). The evaluated T_Bs originate from four days with purely convective cloud cover during the FESSTVaL campaign in summer 2021. The whiskers mark the $2.5\,\%$ and $97.5\,\%$ quantiles.

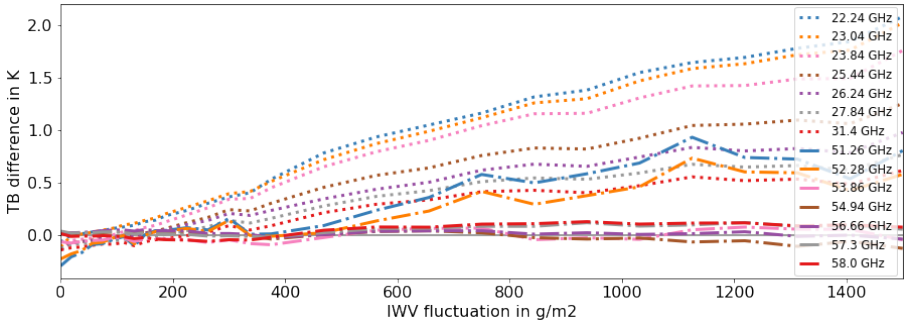

Figure 6. Channelwise statistics of cleared observation (T_B) minus interpolated observation ($T_{B-interpol}$, see eq. 3 and Fig. 4) plotted against $IWV_{fluct} := IWV(t) - IWV_{interpol}(t)$ (Eq. (4)). The evaluated data were obtained during four days with purely convective cloud formation during the FESSTVaL campaign in summer 2021.

To restrict the analysis to distinct cloud passages and to exclude cases dominated by air-mass changes, two filters were applied. First, only cloud passages with durations between $1\,min$ and $1\,h$ were retained. Second, the maximum liquid water path was required to exceed $10\,g\,m^{-2}$. After applying these filters, 35 individual cloud passages remained.

The resulting dataset comprises $7\,h$ of cloudy-sky observations at $1\,s$ resolution. The mean cloud duration is $16\,min$. The average maximum liquid water path per cloud is $50\,g\,m^{-2}$, while the median is $22\,g\,m^{-2}$. Only one case exceeds $200\,g\,m^{-2}$, so the results for $LWP > 200\,g\,m^{-2}$ are of limited statistical significance. Across the channels between 22 and $53\,GHz$, cloud liquid water increases the observed T_Bs by approximately 4 to $9\,K$ per $100\,g\,m^{-2}$. These values characterize the dataset and show that the analyzed cloud passages are sufficiently pronounced to evaluate the retrieval.

The interpolated brightness temperature $T_{B-interpol}$ used as reference is defined as

$$T_{B-interpol} := T_B(t_{start}) + \frac{T_B(t_{end}) - T_B(t_{start})}{t_{end} - t_{start}} \cdot (t - t_{start}) \tag{3}$$

https://doi.org/10.5194/egusphere-2026-2264
Preprint. Discussion started: 8 July 2026

where t_{start} denotes the start and t_{end} the end of the cloud passage.

Figure 5 summarizes the differences of observed and cleared T_Bs relative to $T_{B-interpol}$. In the K-band, Clearing-R_{ERA5} reduces the median difference from typically about $0.3\,K$ to below $0.1\,K$ and decreases the STD from 1.0–$1.7\,K$ to below $0.5\,K$. In the V-band below $54\,GHz$, a similar improvement is found, although the remaining STD is somewhat larger, reaching up to $0.8\,K$. Above $54\,GHz$, however, the median difference is essentially unchanged, and the STD increases slightly by 0.02–$0.04\,K$ ($12\,\%$–$36\,\%$). Thus, in zenith, Clearing-R_{ERA5} effectively removes the liquid-water signal below about $56\,GHz$, while at higher frequencies it introduces a small additional random error without clear benefit.

Frequency in GHz	22.24	23.04	23.84	25.44	26.24	27.84	31.40	51.26	52.28	53.86	54.94	56.66	57.30	58.00
Correlation	0.73	0.73	0.67	0.57	0.50	0.42	0.32	0.24	0.19	0.05	-0.05	0.02	0.02	0.06

Table 8. Correlation of zenith $T_{B-diff} := T_{B-cleared} - T_{B-interpol}$ and $IWV_{fluct} := IWV - IWV_{interpol}$ during cases with convective cloud passage.

To examine the residual differences after cloud clearing, Fig. 6 relates $T_{B-cleared} - T_{B-interpol}$ to fluctuations in integrated water vapor. The fluctuation of integrated water vapor is defined as

$$IWV_{fluct} := IWV(t) - IWV_{interpol} = IWV(t) - \left(IWV(t_{start}) + \frac{IWV(t_{end}) - IWV(t_{start})}{t_{end} - t_{start}} \cdot (t - t_{start}) \right) \tag{4}$$

where $IWV(t)$ is the manufacturer-provided level-2 retrieval, and $IWV_{interpol}$ is defined analogously to $T_{B-interpol}$.

For several channels, especially in the K-band, the residual T_B differences show an approximately linear dependence on IWV_{fluct}. This behavior is consistent with the correlations listed in Table 8, which are highest in the low-frequency channels and decrease toward the V-band. A plausible explanation is that convective clouds are accompanied by small but systematic changes in temperature and humidity, for example, through moist adiabatic ascent, that are not represented by the linear interpolation. The systematic differences are therefore consistent with meteorological variability during cloud passage rather than with a systematic error of Clearing-R_{ERA5}.

Overall, the aggregated case studies show that Clearing-R_{ERA5} yields plausible cleared T_Bs for real observations. The retrieval removes most of the liquid-water-induced signal in the K-band and lower V-band, while the remaining residuals can be largely explained by atmospheric variability during cloud passage. This provides the basis for the following analysis of the impact of cloud clearing on O-B statistics.

3.2.2 Impact of cloud clearing on observation error

To quantify the impact of cloud clearing on the observation error, we separately clear the observed T_Bs and background T_Bs in the O-B statistics introduced in Sect. 3.1.3. To achieve this, we remove the T_B-contribution of cloud liquid water (see Fig. 1) with Clearing-R_{ERA5} and, consistently, remove liquid water from the ICON-D2 profiles prior to the radiative transfer simulations. The resulting statistics represent an “artificial clear-sky” scenario that we directly compare to both native clear-sky and native cloudy-sky conditions.

https://doi.org/10.5194/egusphere-2026-2264
Preprint. Discussion started: 8 July 2026

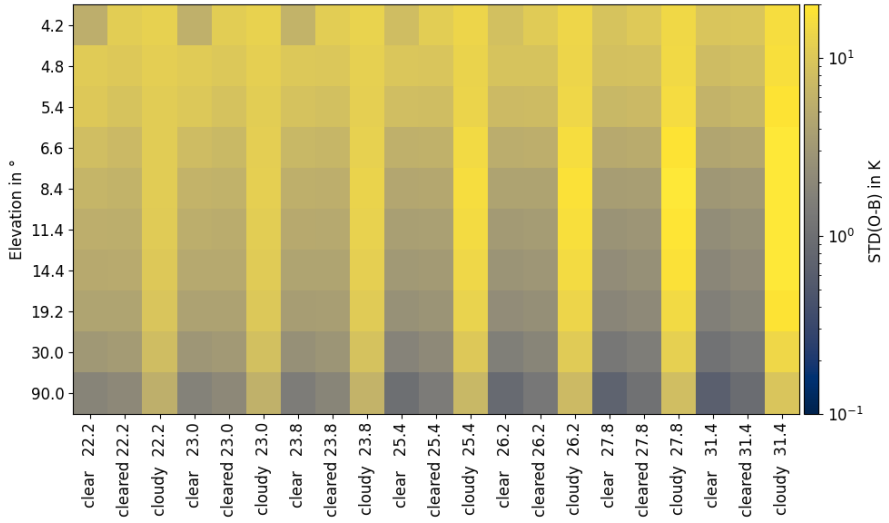

Figure 7. Channelwise (x-axis) and elevation-wise (y-axis) **standard deviation** (color scale, logarithmic scale) of observation (DWDHAT) minus background (ICON-D2) for the K-band. We categorized the statistics into "native clear-sky" (clear), "artificial clear-sky" (cleared), and "native cloudy-sky" (cloudy). The statistics represent 20 months of data from May 2021 – April 2023. lbl_rt_py (Löffler et al., 2025) was used to calculate the model equivalent T_Bs, see Sect. 2.3. Numerical values are listed in Table A2.

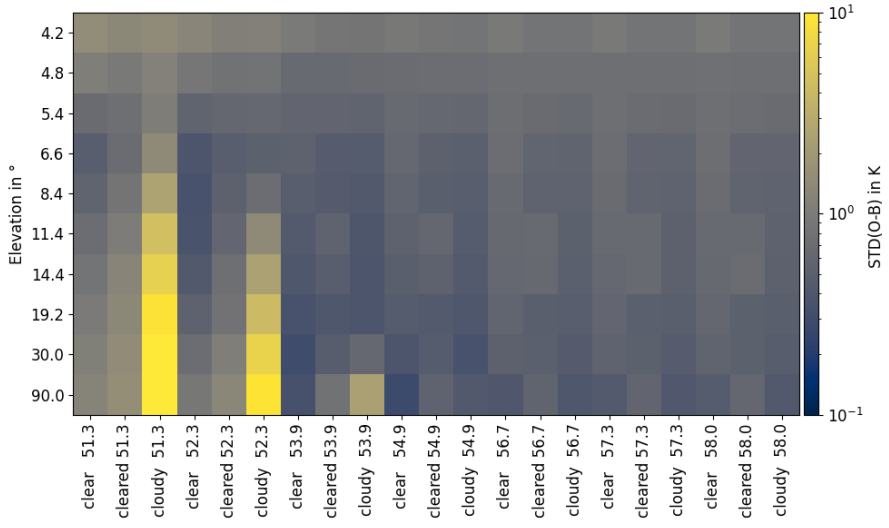

Figure 8. As Fig. 7 for the V-band.

415 In the K-band, all channels and elevation angles are strongly affected by liquid water clouds. As shown in Fig. 7, cloudy-sky O-B STD is substantially larger than under clear-sky conditions. Applying Clearing-R$_{ERA5}$ reduces this excess variability

https://doi.org/10.5194/egusphere-2026-2264
Preprint. Discussion started: 8 July 2026

notably. Across all channels and elevations, the cloudy-sky O-B STD is reduced by typically $60 - 90\,\%$, with a maximum reduction of $22\,K$. After cloud clearing, the remaining O-B STD is close to the native clear-sky level, generally within $0.4\,K$. In several low-elevation and low-frequency cases (e.g. 22–$24\,GHz$), the cleared O-B STD is even slightly lower than the native clear-sky STD.

These results show that Clearing-R$_{ERA5}$ effectively reduces the random observation error (sect. 2.6) in the K-band, namely error of representiveness introduced by cloud liquid water. The resulting O-B statistics indicate that, after clearing, cloudy observations have a representativeness comparable to clear-sky observations.

In the V-band, the impact of cloud liquid water is more limited and depends strongly on channel and elevation (Fig. 8). For channel–elevation combinations with O-B statistics sensitive to liquid water (primarily below about $54\,GHz$), Clearing-R$_{ERA5}$ reduces the O-B STD in a similar way as in the K-band, although the absolute effect is smaller. In contrast, for channel–elevation combinations for which O-B statistics are largely insensitive to liquid water, the cloudy-sky O-B STD is already close to or even below the clear-sky value. In these cases, applying Clearing-R$_{ERA5}$ introduces an increase in STD of up to $0.2\,K$ (up to $38\,\%$).

This behavior indicates that the retrieval's random error becomes relevant when the atmospheric signal of liquid water is weak. Consequently, Clearing-R$_{ERA5}$ provides a clear benefit only where cloud liquid water contributes notably to the O-B standard deviation. In practice, this restricts its useful application to the K-band and the lower V-band ($51.26 - 53.86\,GHz$), while no benefit is obtained in the upper V-band ($54.94 - 58.0\,GHz$).

Overall, these results demonstrate that cloud clearing can reduce the random component of O-B differences in cloudy conditions to near clear-sky levels in the relevant frequency range. This substantial reduction in the approximation of the observation error highlights the potential of Clearing-R$_{ERA5}$ to provide more representative MWR observations for data assimilation in conditions that would otherwise be strongly affected by cloud liquid water.

4 Conclusions

This study aims to improve the representativeness of observed MWR T$_B$s in cloudy-sky conditions relative to predicted (ICON-D2) T$_B$s for data assimilation. Typically, the presence of clouds leads to large random differences between observed and background T$_B$s, which are challenging to handle in data assimilation systems (Geer and Bauer, 2011). So far, data assimilation suppresses the influence of cloud-affected observations or rejects them completely (Vural et al., 2024; Ikuta et al., 2025). To exploit T$_B$s in cloudy cases at arbitrary viewing directions for data assimilation, we developed two novel, complementary retrieval approaches: the cloud detection retrieval, Cloud-R$_{ERA5}$, and the cloud-clearing retrieval, Clearing-R$_{ERA5}$.

We demonstrate that our multi-angle neural-network-based retrieval, Cloud-R$_{ERA5}$, identifies all clouds relevant for data assimilation down to $4.8\,°$ elevation, while reducing the false alarm rate relative to STD30 (De Angelis et al., 2017) and STD6, both building on established cloud detection schemes applicable to zenith observations only. In absolute numbers, this translates to a reduction of the detected cloud cover with respect to STD30 by $12\,\%$ while the STD of clear-sky O-B increases by less than $5\,\%$ within the 2-year analysis period. The reduction of apparent cloud cover from STD30 to Cloud-R$_{ERA5}$ is especially

https://doi.org/10.5194/egusphere-2026-2264
Preprint. Discussion started: 8 July 2026

pronounced in summer due to more frequent transitions between cloudy and clear scenes, which Cloud-R_{ERA5} resolves more accurately.

In addition, this study pioneers the potential of a cloud clearing retrieval, Clearing-R_{ERA5}, which is also applicable to arbitrary viewing directions, to reduce the large random O-B differences in the presence of liquid water clouds for MWRs. For one, the analysis of several cumuliform cloud cases demonstrates that Clearing-R_{ERA5} significantly reduces the T_B difference to interpolated clear-sky observations below $56\,GHz$. But even more, O-B statistics show that Clearing-R_{ERA5} effectively reduces the cloudy-sky O-B STD to only $0.1\,K \pm 0.4\,K$ above the STD of native clear-sky, which is thereby mean (median) $61\,\%$ ($69\,\%$) less than the initial STD of cloudy-sky O-B in channels between $22\,GHz$ and $53\,GHz$. As the O-B STD is a common estimator for the observation error (Geer and Bauer, 2011), cloud clearing could double the effect of assimilating zenith MWR T_B observations and contribute to the assimilation of off-zenith MWR T_B observations as well.

Overall, the results show that ERA5-based neural network retrievals can be successfully used for both cloud detection and cloud clearing in a data-assimilation context. Cloud-R_{ERA5} provides a reliable cloud detection without adversely influencing the clear-sky observation error, while Clearing-R_{ERA5} reduces the random cloudy-sky observation error to near clear-sky levels in the channels affected by liquid water clouds. These results, and the retrievals' low requirements for additional instrumentation, are a promising step towards the broader direct assimilation of MWR T_Bs, including observations at lower elevation angles.

Some limitations should be kept in mind. The analysis is based on a single site, and no independent reference dataset is available to definitively validate all cloud detections and cleared T_Bs. In addition, the benefit of cloud clearing is not uniform across all channels, which underlines the need for channel- and elevation-dependent application. Future work should assess the suitability of the discussed retrievals across different climate zones and at different heights above sea level, and investigate the assimilation of cleared MWR observations using 1DVAR methods or directly in numerical weather prediction systems.

Code and data availability. The ERA5 hourly data on pressure levels, which we used in this study, are available through the Copernicus Climate Data Store (**CDS**) under https://doi.org/10.24381/cds.bd0915c6 (Hersbach et al., 2023).
The MWR observations and products recorded and produced during the FESSTVaL Campaign are available under https://doi.org/10.25592/uhhfdm.10198 (Löhnert et al., 2022).
The code used for radiative transfer calculations is available under https://doi.org/10.5281/zenodo.16919242 (Löffler et al., 2025)
The microwave radiometer brightness temperature data used in this study are available from the Aerosol, Clouds and Trace Gases Research Infrastructure (ACTRIS) Data Center using the following link: https://doi.org/10.60656/a6a3fc626e004c94.
The ICON-D2 model backgrounds are accessible after registration from the DWD database through the PAMORE interface (https://www.dwd.de/EN/ourservices/pamore/pamore).

Author contributions. **Moritz Löffler:** methodology; formal analysis; investigation; software; data curation; formal analysis; visualization; writing - original draft; writing – review and editing.

https://doi.org/10.5194/egusphere-2026-2264
Preprint. Discussion started: 8 July 2026

Christine Knist: data curation; resources; conceptualization; supervision; writing – review and editing.

Bernhard Pospichal: conceptualization; supervision; writing – review and editing.

Ulrich Löhnert: conceptualization; project administration; supervision; writing – review and editing.

Competing interests. The authors declare no conflicts of interest regarding this manuscript.

Acknowledgements. The authors gratefully thank Ronny Leinweber (German Meteorological Service, MOL-RAO) for setting up and maintaining the MWR data processing; Annika Schomburg (German Meteorological Service, Research and Development), Jasmin Vural (Météo-France, GMAP) for their support and helpful discussions concerning data assimilation; Ulrich Görsdorf (German Meteorological Service, MOL-RAO) for helpful discussions on liquid cloud detection in CloudNet as a possible reference; and finally Tobias Marke (University of Cologne) and Dominico Chimini (National Research Council of Italy (CNR-IMAA) and CETEMPS, University of L'Aquila) for supplying independent radiative transport calculations as a verification of the code used in this study.

The authors wish to acknowledge the ACTRIS (Aerosol, Clouds, and Trace Gases Research Infrastructure) for its essential role in providing access to high-quality data, facilities, and technical support that were integral to the execution of this research. We acknowledge the Finnish Meteorological Institute for hosting the microwave radiometer brightness temperature dataset, available for download from https://cloudnet.fmi.fi.

FESSTVaL was carried out in 2021 as a measurement campaign within the Hans Ertel Centre for Weather Research (Hans-Ertel-Zentrum für Wetterforschung; HErZ), a German research network of universities, research institutions, and the German Meteorological Service (Deutscher Wetterdienst; DWD), funded by the Federal Ministry of Transport (Bundesministerium für Verkehr; BMV).

The authors used AI-based tools, including ChatGPT (OpenAI) and Microsoft Copilot, to improve the clarity and readability of parts of the manuscript. All scientific content, analysis, and conclusions were developed and verified by the authors.

https://doi.org/10.5194/egusphere-2026-2264
Preprint. Discussion started: 8 July 2026

		Cloud R_{ERA5}		Cloud R_{ERA5} FOGHAT		STD6		STD30		LWP R_{RS} DWDHAT		LWP R_{RS} FOGHAT	
Cloud R_{ERA5}				91	9	70	30	54	46	94	6	97	3
				6	94	10	90	7	93	20	80	25	75
Cloud R_{ERA5} FOGHAT		96	4			77	23	63	37	95	5	97	3
		13	87			12	88	7	93	23	77	30	70
STD6		87	13	89	11			74	26	99	1	99	1
		24	76	26	74			0	100	28	72	39	61
STD30		89	11	92	8	100	0			99	1	100	0
		32	68	35	68	15	85			38	62	49	51
LWP DWDHAT		81	19	85	15	70	30	52	48			98	2
		6	94	8	92	1	99	0	100			15	85
LWP FOGHAT		86	14	81	19	72	28	57	43	92	8		
		7	93	5	95	1	99	0	100	4	96		

Table A1. Recall matrices of comparisons between zenith cloud detection algorithms evaluated in this study. The structure of this table is as demonstrated in Table 4, with the "true" reference on the left side. LWP-based cloud detection uses $LWP = 5\,gm^{-2}$ as the detection limit.

Appendix A: Appendix A

https://doi.org/10.5194/egusphere-2026-2264
Preprint. Discussion started: 8 July 2026

elevation	22.2 GHz			23.0 GHz			23.8 GHz			25.4 GHz			26.2 GHz			27.8 GHz			31.4 GHz		
angle	clear	cleared	cloudy	clear	cleared	cloudy	clear	cleared	cloudy	clear	cleared	cloudy	clear	cleared	cloudy	clear	cleared	cloudy	clear	cleared	cloudy
4.2	5.52	11.33	12.37	5.76	11.21	12.43	6.07	11.21	12.77	7.72	11.21	13.65	8.23	10.89	13.90	9.03	10.38	14.55	9.48	9.66	15.96
4.8	10.97	10.14	11.66	10.79	10.07	11.73	10.00	9.70	12.00	9.56	9.38	13.13	9.00	9.05	13.66	8.47	8.61	14.79	7.68	8.09	16.88
5.4	10.30	8.95	11.10	9.93	8.75	11.26	8.92	8.29	11.70	7.96	7.78	13.34	7.40	7.50	14.15	6.87	7.17	15.70	6.19	6.81	18.29
6.6	8.03	7.21	11.03	7.68	7.06	11.47	6.85	6.59	12.41	5.74	5.81	14.99	5.32	5.46	16.24	4.87	5.03	18.34	4.36	4.56	21.66
8.4	6.46	6.10	11.17	6.24	5.94	11.74	5.63	5.46	12.96	4.48	4.52	15.95	4.06	4.14	17.39	3.54	3.66	19.73	3.01	3.21	23.38
11.4	5.54	5.35	10.75	5.36	5.20	11.34	4.80	4.72	12.52	3.67	3.76	15.32	3.27	3.39	16.64	2.72	2.90	18.87	2.29	2.54	22.37
14.4	4.88	4.90	10.24	4.70	4.73	10.79	4.17	4.23	11.82	3.11	3.29	14.25	2.75	2.96	15.37	2.27	2.52	17.33	1.93	2.21	20.59
19.2	4.18	4.21	9.42	4.02	4.06	9.93	3.52	3.60	10.77	2.57	2.76	12.72	2.26	2.46	13.63	1.86	2.08	15.26	1.58	1.83	18.17
30.0	3.06	3.32	7.86	2.93	3.22	8.26	2.50	2.81	8.83	1.76	2.07	10.15	1.54	1.81	10.78	1.25	1.50	11.98	1.07	1.31	14.32
90.0	1.78	2.04	5.57	1.69	2.02	5.79	1.42	1.83	6.18	0.98	1.41	6.89	0.86	1.25	7.27	0.69	1.04	7.97	0.62	0.91	9.40

elevation	51.3 GHz			52.3 GHz			53.9 GHz			54.9 GHz			56.7 GHz			57.3 GHz			58.0 GHz		
angle	clear	cleared	cloudy	clear	cleared	cloudy	clear	cleared	cloudy	clear	cleared	cloudy	clear	cleared	cloudy	clear	cleared	cloudy	clear	cleared	cloudy
4.2	1.52	1.35	1.44	1.28	1.11	1.12	0.95	0.85	0.84	0.93	0.85	0.83	0.95	0.83	0.83	0.95	0.83	0.83	0.95	0.83	0.82
4.8	1.06	0.94	1.13	0.87	0.79	0.81	0.65	0.66	0.67	0.68	0.70	0.69	0.73	0.73	0.73	0.75	0.73	0.73	0.76	0.74	0.73
5.4	0.67	0.75	1.04	0.56	0.60	0.60	0.58	0.57	0.56	0.65	0.62	0.60	0.72	0.67	0.65	0.73	0.68	0.66	0.74	0.69	0.67
6.6	0.47	0.68	1.42	0.38	0.48	0.51	0.53	0.46	0.45	0.61	0.52	0.50	0.69	0.57	0.56	0.71	0.58	0.57	0.72	0.58	0.57
8.4	0.55	0.85	2.48	0.35	0.52	0.70	0.48	0.44	0.42	0.57	0.50	0.47	0.66	0.55	0.53	0.67	0.55	0.54	0.68	0.56	0.55
11.4	0.70	1.02	4.57	0.36	0.59	1.43	0.43	0.54	0.39	0.53	0.60	0.45	0.63	0.64	0.51	0.65	0.65	0.52	0.66	0.65	0.53
14.4	0.83	1.25	6.55	0.42	0.73	2.46	0.39	0.47	0.37	0.49	0.52	0.43	0.60	0.63	0.50	0.62	0.66	0.52	0.63	0.68	0.52
19.2	0.97	1.36	8.99	0.52	0.80	4.18	0.35	0.39	0.37	0.45	0.43	0.40	0.57	0.49	0.48	0.59	0.50	0.49	0.60	0.51	0.49
30.0	1.09	1.48	11.54	0.69	1.06	6.94	0.30	0.46	0.62	0.38	0.45	0.35	0.51	0.50	0.44	0.54	0.51	0.46	0.56	0.51	0.47
90.0	1.20	1.59	11.79	0.90	1.31	9.23	0.34	0.79	2.36	0.28	0.54	0.42	0.40	0.55	0.39	0.43	0.58	0.41	0.45	0.60	0.42

Table A2. Channelwise and elevation-wise STD of observation (DWD-HAT) minus background (ICON-D2) from May 2021 – April 2023. Cleared cases only include data from cloudy-sky situations.

https://doi.org/10.5194/egusphere-2026-2264
Preprint. Discussion started: 8 July 2026

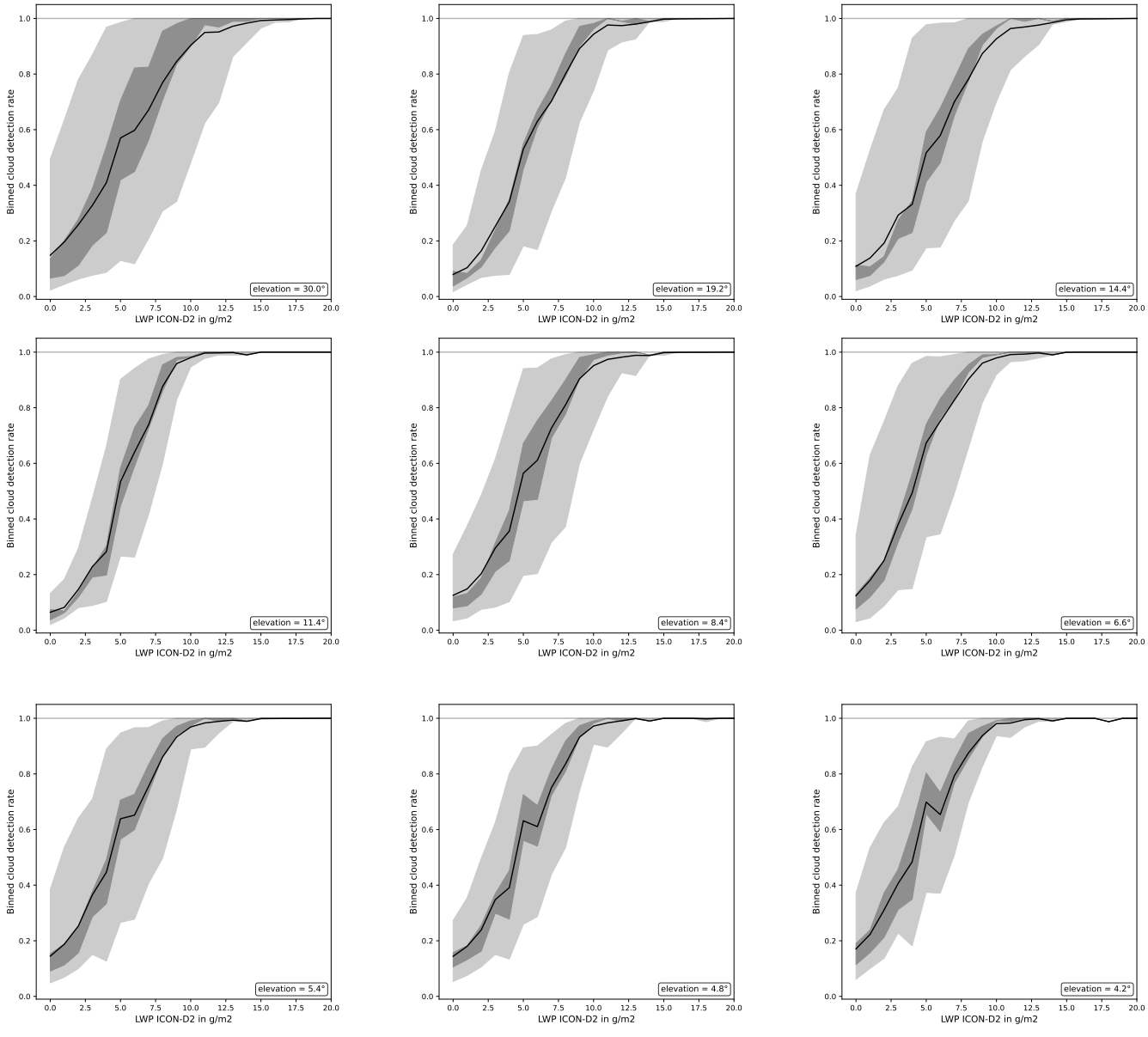

Figure A1. Binned cloud detection rates (eq. 2, POD_{local}) of Cloud-R_{ERA5} tested on two years of ICON-D2 background T_Bs and LWPs. The dark shading indicates the 25th and 75th percentiles, the light shading indicates the 5th and 95th percentiles. The percentiles are determined by biasing the input T_Bs with a Monte Carlo method.

https://doi.org/10.5194/egusphere-2026-2264
Preprint. Discussion started: 8 July 2026

References

Ahn, M.-H., Han, D., Won, H., and Morris, V.: A cloud detection algorithm using the downwelling infrared radiance measured by an infrared pyrometer of the ground-based microwave radiometer, Atmospheric Measurement Techniques, 8, 553–566, 2015.

Anderson, E. and Järvinen, H.: Variational quality control, Quarterly Journal of the Royal Meteorological Society, 125, 697–722, 1999.

Böck, T., Pospichal, B., and Löhnert, U.: Measurement uncertainties of scanning microwave radiometers and their influence on temperature profiling, Atmospheric Measurement Techniques, 17, 219–233, 2024.

Böck, T., Löffler, M., Marke, T., Pospichal, B., Knist, C., and Löhnert, U.: Instrument uncertainties of network-suitable ground-based microwave radiometers: overview, quantification, and mitigation strategies, EGUsphere, 2025, 1–32, https://doi.org/10.5194/egusphere-2025-1727, 2025.

Cao, Y., Shi, B., Zhao, X., Yang, T., and Min, J.: Direct Assimilation of Ground-Based Microwave Radiometer Clear-Sky Radiance Data and Its Impact on the Forecast of Heavy Rainfall, Remote Sensing, 15, https://doi.org/10.3390/rs15174314, 2023.

Cimini, D., Hewison, T. J., Martin, L., Güldner, J., Gaffard, C., and Marzano, F. S.: Temperature and humidity profile retrievals from ground-based microwave radiometers during TUC, Meteorologische Zeitschrift, 15, 45–56, https://doi.org/10.1127/0941-2948/2006/0099, 2006.

Cimini, D., Rosenkranz, P. W., Tretyakov, M. Y., Koshelev, M. A., and Romano, F.: Uncertainty of atmospheric microwave absorption model: impact on ground-based radiometer simulations and retrievals, Atmospheric Chemistry and Physics, 18, 15 231–15 259, 2018.

Cimini, D., Haeffelin, M., Kotthaus, S., Löhnert, U., Martinet, P., O'Connor, E., Walden, C., Coen, M. C., and Preissler, J.: Towards the profiling of the atmospheric boundary layer at European scale—introducing the COST Action PROBE, Bulletin of Atmospheric Science and Technology, 1, 23–42, 2020.

Crewell, S. and Löhnert, U.: Accuracy of cloud liquid water path from ground-based microwave radiometry 2. Sensor accuracy and synergy, Radio Science, 38, 7–1, 2003.

De Angelis, F., Cimini, D., Hocking, J., Martinet, P., and Kneifel, S.: RTTOV-gb–adapting the fast radiative transfer model RTTOV for the assimilation of ground-based microwave radiometer observations, Geoscientific Model Development, 9, 2721–2739, 2016.

De Angelis, F., Cimini, D., Löhnert, U., Caumont, O., Haefele, A., Pospichal, B., Martinet, P., Navas-Guzmán, F., Klein-Baltink, H., Dupont, J.-C., et al.: Long-term observations minus background monitoring of ground-based brightness temperatures from a microwave radiometer network, Atmospheric Measurement Techniques, 10, 3947–3961, 2017.

Ellison, W.: Permittivity of pure water, at standard atmospheric pressure, over the frequency range–25thz and the temperature range–100 c, Journal of physical and chemical reference data, 36, 1–18, 2007.

Geer, A. J. and Bauer, P.: Observation errors in all-sky data assimilation, Quarterly Journal of the Royal Meteorological Society, 137, 2024–2037, 2011.

Geer, A. J., Bauer, P., and English, S. J.: Assimilating AMSU-A temperature sounding channels in the presence of cloud and precipitation, vol. 670, European Centre for Medium-Range Weather Forecasts Reading, UK, 2012.

Hersbach, H., Bell, B., Berrisford, P., Biavati, G., Horányi, A., Muñoz Sabater, J., Nicolas, J., Peubey, C., Radu, R., Rozum, I., Schepers, D., Simmons, A., Soci, C., Dee, D., and Thépaut, J.-N.: ERA5 hourly data on pressure levels from 1940 to present. Copernicus Climate Change Service (C3S) Climate Data Store (CDS), https://doi.org/10.24381/cds.bd0915c6, accessed on 10-05-2023, 2023.

Hocke, K., Navas Guzmán, F., Cossu, F., and Mätzler, C.: Cloud fraction of liquid water clouds above Switzerland over the last 12 years, Climate, 4, 48, 2016.

https://doi.org/10.5194/egusphere-2026-2264
Preprint. Discussion started: 8 July 2026

Hohenegger, C., Ament, F., Beyrich, F., Löhnert, U., Rust, H., Bange, J., Böck, T., Böttcher, C., Boventer, J., Burgemeister, F., et al.: Fesstval: The field experiment on submesoscale spatio-temporal variability in lindenberg, Bulletin of the American Meteorological Society, 104, E1875–E1892, 2023.

Hunt, B. R., Kostelich, E. J., and Szunyogh, I.: Efficient data assimilation for spatiotemporal chaos: A local ensemble transform Kalman filter, Physica D: Nonlinear Phenomena, 230, 112–126, 2007.

Ikuta, Y., Seko, H., Yoshimoto, K., Yamamoto, K., Kawabata, T., Ishimoto, H., Araki, K., Tajiri, T., and Shimizu, S.: Impact of direct assimilation of ground-based microwave radiometer on numerical weather prediction: Accounting for interchannel observation error correlations, Quarterly Journal of the Royal Meteorological Society, p. e5067, 2025.

Illingworth, A. J., Hogan, R. J., O'Connor, E., Bouniol, D., Brooks, M. E., Delanoé, J., Donovan, D. P., Eastment, J. D., Gaussiat, N., Goddard, J. W. F., Haeffelin, M., Baltink, H. K., Krasnov, O. A., Pelon, J., Piriou, J.-M., Protat, A., Russchenberg, H. W. J., Seifert, A., Tompkins, A. M., van Zadelhoff, G.-J., Vinit, F., Willén, U., Wilson, D. R., and Wrench, C. L.: Cloudnet: Continuous Evaluation of Cloud Profiles in Seven Operational Models Using Ground-Based Observations, Bulletin of the American Meteorological Society, 88, 883 – 898, https://doi.org/10.1175/BAMS-88-6-883, 2007.

Illingworth, A. J., Cimini, D., Haefele, A., Haeffelin, M., Hervo, M., Kotthaus, S., Löhnert, U., Martinet, P., Mattis, I., O'connor, E., et al.: How can existing ground-based profiling instruments improve European weather forecasts?, Bulletin of the American Meteorological Society, 100, 605–619, 2019.

Knist, C. and Görsdorf, U.: Custom collection of MWR brightness temperature data from Lindenberg between 1 May 2021 and 30 Apr 2023, https://doi.org/10.60656/a6a3fc626e004c94, 2026.

Levis, C., Johnson, J. T., and Teixeira, F. L.: Radiowave propagation: physics and applications, John Wiley & Sons, 2010.

Löhnert, U. and Crewell, S.: Accuracy of cloud liquid water path from ground-based microwave radiometry 1. Dependency on cloud model statistics, Radio Science, 38, 2003.

Löhnert, U., van Meijgaard, E., Baltink, H. K., Groß, S., and Boers, R.: Accuracy assessment of an integrated profiling technique for operationally deriving profiles of temperature, humidity, and cloud liquid water, Journal of Geophysical Research: Atmospheres, 112, 2007.

Löffler, M.: HATPRO MWR rain flagging and radome status monitoring, https://doi.org/10.5281/zenodo.10984797, 2024.

Löffler, M., Maschwitz, G., and Löhnert, U.: Line-by-Line Radiative Transfer Model in python (lbl_rt_py), https://doi.org/10.5281/zenodo.16919242, 2025.

Löhnert, U., Knist, C., Böck, T., and Pospichal, B.: Microwave Radiometer Observations during FESSTVaL 2021, https://doi.org/10.25592/uhhfdm.10198, Project: FESSTVaL (Field Experiment on submesoscale spatio-temporal variability in Lindenberg), a measurement campaign initiated by the Hans-Ertel-Center for Weather Research., 2022.

Marke, T., Ebell, K., Löhnert, U., and Turner, D. D.: Statistical retrieval of thin liquid cloud microphysical properties using ground-based infrared and microwave observations, Journal of Geophysical Research: Atmospheres, 121, 14–558, 2016.

Marke, T., Löhnert, U., Schemann, V., Schween, J. H., and Crewell, S.: Detection of land-surface-induced atmospheric water vapor patterns, Atmospheric Chemistry and Physics, 20, 1723–1736, https://doi.org/10.5194/acp-20-1723-2020, 2020.

Martinet, P., Dabas, A., Donier, J.-M., Douffet, T., Garrouste, O., and Guillot, R.: 1D-Var temperature retrievals from microwave radiometer and convective scale model, Tellus A: Dynamic Meteorology and Oceanography, 67, 27 925, 2015.

https://doi.org/10.5194/egusphere-2026-2264
Preprint. Discussion started: 8 July 2026

Martinet, P., Cimini, D., Burnet, F., Ménétrier, B., Michel, Y., and Unger, V.: Improvement of numerical weather prediction model analysis during fog conditions through the assimilation of ground-based microwave radiometer observations: a 1D-Var study, Atmospheric Measurement Techniques, 13, 6593–6611, https://doi.org/10.5194/amt-13-6593-2020, 2020.

Meunier, V., Löhnert, U., Kollias, P., and Crewell, S.: Biases caused by the instrument bandwidth and beam width on simulated brightness temperature measurements from scanning microwave radiometers, Atmospheric Measurement Techniques, 6, 1171–1187, 2013.

National Research Council, Division on Earth and Life Studies, Board on Atmospheric Sciences, and Committee on Developing Mesoscale Meteorological Observational Capabilities to Meet Multiple National Needs: Observing weather and climate from the ground up: A nationwide network of networks, National Academies Press, 2009.

Pedregosa, F., Varoquaux, G., Gramfort, A., Michel, V., Thirion, B., Grisel, O., Blondel, M., Prettenhofer, P., Weiss, R., Dubourg, V., Vanderplas, J., Passos, A., Cournapeau, D., Brucher, M., Perrot, M., and Duchesnay, E.: Scikit-learn: Machine Learning in Python, Journal of Machine Learning Research, 12, 2825–2830, 2011.

Rose, T., Crewell, S., Löhnert, U., and Simmer, C.: A network suitable microwave radiometer for operational monitoring of the cloudy atmosphere, Atmospheric research, 75, 183–200, 2005.

Rosenkranz, P.: Line-by-line microwave radiative transfer (non-scattering), https://doi.org/10.21982/M81013, 2022.

Rüeger, J. M.: Refractive indices of light, infrared and radio waves in the atmosphere, School of Surveying and Spatial Information Systems, University of New South Wales, 2002.

Rüfenacht, R., Haefele, A., Pospichal, B., Cimini, D., Bircher-Adrot, S., Turp, M., and Sugier, J.: EUMETNET opens to microwave radiometers for operational thermodynamical profiling in Europe, 2021.

Salmi, A., Ikonen, J., and Oyj, V.: Piezoelectric precipitation sensor from Vaisala, in: WMO Technical Conference on Instruments and Methods of Observation (TECO-2005), Bucharest, Romania, pp. 4–7, Citeseer, 2005.

Shuvalova, J., Chubarova, N., and Shatunova, M.: Cloud Characteristics and Their Effects on Solar Irradiance According to the ICON Model, CLOUDNET and BSRN Observations, Atmosphere, 14, 1769, 2023.

Simmer, C.: Satellitenfernerkundung hydrologischer Parameter der Atmosphäre mit Mikrowellen, Verlag Dr. Kovač, 1994.

Szegedy, C.: Intriguing properties of neural networks, arXiv preprint arXiv:1312.6199, 2013.

Turner, D.: Improved ground-based liquid water path retrievals using a combined infrared and microwave approach, Journal of Geophysical Research: Atmospheres, 112, 2007.

Turner, D. D. and Löhnert, U.: Ground-based temperature and humidity profiling: Combining active and passive remote sensors, Atmospheric Measurement Techniques, 14, 3033–3048, 2021.

Vural, J., Merker, C., Löffler, M., Leuenberger, D., Schraff, C., Stiller, O., Schomburg, A., Knist, C., Haefele, A., and Hervo, M.: Improving the representation of the atmospheric boundary layer by direct assimilation of ground-based microwave radiometer observations, Quarterly Journal of the Royal Meteorological Society, 2024.

Zängl, G., Reinert, D., Rípodas, P., and Baldauf, M.: The ICON (ICOsahedral Non-hydrostatic) modelling framework of DWD and MPI-M: Description of the non-hydrostatic dynamical core, Quarterly Journal of the Royal Meteorological Society, 141, 563–579, 2015.